PAPER

Dynamic model for an ensemble of interacting irradiation-induced defects in a macroscopic sample

IOP Publishing Modelling and Simulation in Materials Science and Engineering
Modelling Simul. Mater. Sci. Eng. **29** (2021) 025004 (24pp) https://doi.org/10.1088/1361-651X/abd014

Dynamic model for an ensemble of interacting irradiation-induced defects in a macroscopic sample

Federico Baraglia[1,3] **and Pui-Wai Ma**[2,*]

[1] Department of Mechanics and Materials, École des Ponts ParisTech, France
[2] United Kingdom Atomic Energy Authority, Culham Science Centre, Oxfordshire OX14 3DB, United Kingdom

E-mail: federico.baraglia@eleves.enpc.fr and Leo.Ma@ukaea.uk

Received 24 August 2020
Accepted for publication 2 December 2020
Published 2 February 2021

Abstract

We develop a dynamic model for the evolution of an ensemble of hundreds of interacting irradiation-induced mobile nanoscale defects in a micrometre size sample. The model uses a Langevin defect dynamics approach coupled to a finite element model, treated using the superposition method. The elastic field of each defect is described by its elastic dipole tensor, and the long-range interaction between defects is treated using the elastic Green's function formalism. The approach circumvents the need to evaluate the elastic energy by means of volume integration, and provides a simple expression for the energy of elastic image interaction between the migrating defects and surfaces of the sample. We discuss the underlying theory, and also the parallelization and coarse-graining numerical algorithms that help speed up simulations. The model addresses the issue of imbalanced forces and moments arising as an artefact of the modified boundary problem associated with the traction free boundary condition. To illustrate applications of the method, we explore the dynamic evolution of an ensemble of interacting dislocation loops of various size and with different Burgers vectors, which proves the feasibility of performing large-scale simulations using the proposed model.

Keywords: elastic dipole tensor, Langevin defect dynamics, finite element method

*Author to whom any correspondence should be addressed.
[3] Federico Baraglia contributed to this work as a part of an internship, supported by the French Embassy in the UK, at the Culham Centre for Fusion Energy, UK Atomic Energy Authority, Culham Science Centre, Oxfordshire OX14 3DB, United Kingdom.

(Some figures may appear in colour only in the online journal)

1. Introduction

Radiation damage in materials due to high energy neutrons is an important consideration for the design of fission and fusion power plants. The choice of materials and their resistance to irradiation greatly affect the performance and the lifetime of reactor components. The change of thermal and mechanical properties due to the evolution of a radiation-induced microstructure can have significant consequences on the safety, maintenance and building cost of a reactor [1, 2]. Predicting the strain, stress and swelling of components during operation requires knowledge about the change of microstructure under irradiation [3], where local deformation of lattice structure stems from the substantial relaxation volume of irradiation defects [4, 5].

Inside a fusion reactor, deuterium–tritium fusion reactions in the hot plasma produce high energy neutrons that penetrate deep into the bulk of reactor components [6, 7], where they initiate atomic collision cascades, resulting in the formation of complex microstructures containing dislocation loops, vacancy clusters, networks of dislocation lines [8–13, 89]. Low fluence irradiation damage in metals generates a variety of localized defects, typically Frenkel pairs, dislocation loops, and voids, which degrade both thermal [14–16] and mechanical [17] properties of plasma facing and structural materials, leading to embrittlement, and limiting the lifetime of reactor components. Fundamentally, the above changes stem from the fact that mechanical and physical properties of metals strongly depend on their microstructure [18].

Molecular dynamics simulations of collision cascades in perfect crystals [8–11] suggest that the statistics of sizes and numbers of vacancy and interstitial defects formed at low dose, below the cascade overlap dose of ~ 0.01 dpa, follow a power-law scaling. This means that a considerable, if not dominant, fraction of defects produced by irradiation is not visible in a transmission electron microscope (TEM) [12, 19, 20]. The fact that the microstructure of an irradiated material contains many defects and defect clusters that are too small to be observed by means of even high resolution experimental methods, makes modelling and simulation a vital tool for understanding the various aspects of microstructural evolution under irradiation that are critical to an informed reactor design effort.

In other molecular dynamics simulations of collision cascades [10, 21], with explicit free surfaces, we observe the formation of vacancy loops near surfaces, suggesting that surfaces attract self-interstitial atom (SIA) defects. Vacancy loops also form during cascade collapse when sequential cascades overlap [22]. Following a cascade collapse, elastic interaction helps trap dislocation loops, preventing their escape to the surface [11, 12, 23]. At the same time, elastic interaction between defects and their elastic images result in that surfaces act as strong sinks for defects [24].

The above evidence suggests that irradiated materials likely contain dense populations of interacting defects. This has important implications for the selection of simulation methodology. The presence of long-range elastic interaction suggests that the movement of any given defect, considered in the context of dynamic evolution of microstructure, depends on the position of a large number of other defects in its neighbourhood. This implies an $\mathcal{O}(N^2)$ naive scaling of the computational cost of execution of each time-step, potentially improvable to $\mathcal{O}(N)$ scaling if the data are efficiently reused. Object kinetic Monte Carlo (okMC) simulations [25–32], commonly applied to simulate the dynamics of irradiation-induced defects, therefore struggle to incorporate elastic interactions efficiently. The correlated motion of defects means that the update time increment also must scale with the number of interacting defects as $1/N$, making the okMC computational cost for elastically interacting defects varying as $\mathcal{O}(N^2)$ at best.

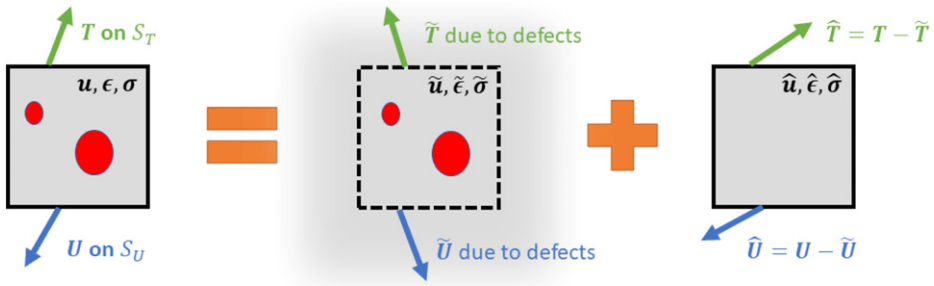

Figure 1. A schematic illustration of the superposition method according to van der Giessen and Needleman [48].

Alternatively, the dynamics of an ensemble of interacting defects at a finite temperature can be modelled using coupled over-damped Langevin equations of motion. These equations describe the effect of temperature on the motion of interacting defects by means of random thermal forces [33]. By recasting the evolution of a system of interacting defects in the Langevin dynamics framework, we can keep a constant time increment while preserving the okMC rules for defect interactions. This gives an improvement in the scaling of computational cost from $\mathcal{O}(N^2)$ to $\mathcal{O}(N)$.

Elastic interaction between the defects can be evaluated using the elastic dipole tensor and Green's function formalism [4, 34–43], where the elements of elastic dipole tensor fully define the field of elastic displacements of a localized defect in the asymptotic far-field limit [44]. This simplifies the evaluation of elastic energy, as performing volume integration of strain and stress fields becomes unnecessary. The elastic dipole tensor formalism has been applied in okMC models to study the point defects diffusion under the influence of the elastic field of a dislocation in iron and vanadium [28, 29] and of an oxide particle in ODS steel [32]. The elastic contribution due to the interaction of defects with the surface of the sample can be evaluated using a finite element model approach [45–47], involving the use of the superposition principle by van der Giessen and Needleman [48].

In this work, we develop a model that in principle can simulate the dynamics of an ensemble of arbitrary defects in a finite size sample, retaining the full complexity of microstructural evolution in an irradiated sample with boundaries at a finite temperature. Knowing the distribution of defects in space as a function of time can help develop practical computational means for evaluating strain, stress and swelling in irradiated reactor components [3].

Below, we summarise the fundamentals of the model and explore examples of simulations of interacting defects. All the formulae are given assuming general anisotropic elasticity, and are not constrained to particular material. It can be extended to arbitrary defects as long as the elastic field of a defect is treated in the elastic dipole tensor approximation [4, 44]. In the application section, we present examples and a numerical implementation using isotropic elasticity. We study loop–loop interactions and the effect of surfaces on the spatial distribution of loops, demonstrating the feasibility of large-scale simulations performed using the model. Tungsten is chosen as a representative example because of its technological relevance in fusion energy and the availability of experimental data.

2. Fundamentals

2.1. Superposition method and its implementation

According to van der Giessen and Needleman [48], a mixed traction-displacement boundary problem describing a finite elastic body can be represented by a superposition of fields defined in an infinite body, and a modified boundary problem (illustrated in figure 1). For a linear elastic body of volume V, with surface boundary $S = S_T \cup S_U$, subject to a traction boundary condition $\mathbf{T}$ on S_T and a displacement boundary condition $\mathbf{U}$ on S_U, the total displacement $\mathbf{u}$, strain $\boldsymbol{\epsilon}$ and stress $\boldsymbol{\sigma}$ fields in V, and traction and displacement on S can be written as a superposition of two fields.

$$\begin{aligned}
\mathbf{u} &= \tilde{\mathbf{u}} + \hat{\mathbf{u}},\\
\boldsymbol{\epsilon} &= \tilde{\boldsymbol{\epsilon}} + \hat{\boldsymbol{\epsilon}},\\
\boldsymbol{\sigma} &= \tilde{\boldsymbol{\sigma}} + \hat{\boldsymbol{\sigma}},\\
\mathbf{T} &= \tilde{\mathbf{T}} + \hat{\mathbf{T}},\\
\mathbf{U} &= \tilde{\mathbf{U}} + \hat{\mathbf{U}},
\end{aligned} \tag{1}$$

where a symbol with a tilde ($\tilde{\circ}$) refers to a quantity in a volume of space that is a part of a continuous infinite medium where the elastic fields can often be calculated using analytical formulae.

This reduces the treatment to solving the so-called modified boundary problem

$$\begin{aligned}
\hat{\mathbf{u}} &= \mathbf{u} - \tilde{\mathbf{u}},\\
\hat{\boldsymbol{\epsilon}} &= \boldsymbol{\epsilon} - \tilde{\boldsymbol{\epsilon}},\\
\hat{\boldsymbol{\sigma}} &= \boldsymbol{\sigma} - \tilde{\boldsymbol{\sigma}},\\
\hat{\mathbf{T}} &= \mathbf{T} - \tilde{\mathbf{T}},\\
\hat{\mathbf{U}} &= \mathbf{U} - \tilde{\mathbf{U}}.
\end{aligned} \tag{2}$$

The governing equations of elasticity for the modified boundary problem are the zero body force condition of mechanical equilibrium

$$\left.\begin{aligned}
\nabla \cdot \hat{\boldsymbol{\sigma}} &= 0\\
\hat{\boldsymbol{\sigma}} &= \mathbf{C} : \hat{\boldsymbol{\epsilon}}\\
\hat{\boldsymbol{\epsilon}} &= \frac{1}{2}(\nabla\hat{\mathbf{u}} + (\nabla\hat{\mathbf{u}})^{\mathrm{T}})
\end{aligned}\right\} \text{in } V, \tag{3}$$

complemented with a boundary condition at surfaces

$$\hat{\boldsymbol{\sigma}} \cdot \mathbf{n} = \hat{\mathbf{T}} \text{ on } S_T, \tag{4}$$

$$\hat{\mathbf{u}} = \hat{\mathbf{U}} \text{ on } S_U. \tag{5}$$

Here $\mathbf{n}$ is the surface normal, $\mathbf{C} = \{C_{\mathrm{ijkl}}\}$ is the fourth rank elastic constant tensor. These equations can be solved numerically using a finite element method (FEM) approach [45–47]. Previous works, coupling discrete dislocation dynamics to FEM [49–52], demonstrate the feasibility and validity of the superposition method.

There is an element of subtlety associated with the boundary part of the problem arising in the context of the superposition method. The total applied force and its torque do not necessarily vanish since $\hat{\mathbf{T}}$ is in general non-zero in equation (4). If $\mathbf{T} = 0$, the total force and torque acting on the body described by the modified boundary problem, and stemming from the boundary conditions, are

$$\int_{S_T} \hat{\mathbf{T}}\,\mathrm{d}S = -\int_{S_T} \tilde{\mathbf{T}}\,\mathrm{d}S \neq 0, \tag{6}$$

$$\int_{S_T} \mathbf{r} \times \hat{\mathbf{T}}\,\mathrm{d}S = -\int_{S_T} \mathbf{r} \times \tilde{\mathbf{T}}\,\mathrm{d}S \neq 0. \tag{7}$$

This is at odds with the expected stationary solution of the mechanical equilibrium problem.

A conventional way of addressing the issue is to impose common sense constraints on the six degrees of freedom of the system, see for example the FEM treatment given in reference [3]. Out of the six degrees of freedom, three describe translations of the body as a whole, and the other three refer to its rotation. To make sure that numerical solvers do not produce a moving and rotating FEM solution, positions of any two points in the body are assumed stationary. However, since the FEM problem involves applied tractions at surfaces given by equation (4), local stress concentrations naturally form near these fixed points. In the context of the problem of dynamics of defects, the presence of any pinning points and stress concentrations is undesirable.

To treat the imbalanced force and torque in a non-singular manner, avoiding the use of pinning points, we introduce a modification to the superposition method. We introduce a fictitious distributed body force $\mathbf{F^f}$ that compensates the effect of tractions in equation (4). This body force should satisfy conditions that

$$\int_{S_T} \hat{\mathbf{T}}\,\mathrm{d}S = -\int_{V} \mathbf{F^f}\,\mathrm{d}V, \tag{8}$$

$$\int_{S_T} \mathbf{r} \times \hat{\mathbf{T}}\,\mathrm{d}S = -\int_{V} \mathbf{r} \times \mathbf{F^f}\,\mathrm{d}V. \tag{9}$$

Since these conditions only involve a volume integral of the body force, there is still freedom associated with the choice of its functional form.

To eliminate translations, we use a uniform body force field. The corresponding expression for the spatially homogeneous body force compensating translations is

$$\mathbf{F^t} = -\frac{1}{V}\oint_{S_T} \hat{\boldsymbol{T}}\,\mathrm{d}S. \tag{10}$$

To eliminate rotations, we assume that the torque associated with tractions acts to turn the system around an axis going through the centre of mass and parallel to the torque vector. In cylindrical coordinates, we find

$$F^r_z = 0, \tag{11}$$

$$F^r_r = 0, \tag{12}$$

$$F^r_\theta = \rho\kappa r, \tag{13}$$

where κ is a constant derived from the condition

$$\oint_V \mathbf{r} \times \mathbf{F^r}\,\mathrm{d}V = -\oint_S \mathbf{r} \times \hat{\boldsymbol{T}}\,\mathrm{d}S. \tag{14}$$

The total density of fictitious body force and its torque are now

$$\mathbf{F}^{\mathbf{f}} = \mathbf{F}^{\mathbf{t}} + \mathbf{F}^{\mathbf{r}}, \tag{15}$$

$$\boldsymbol{\tau}^{f} = \mathbf{r} \times (\mathbf{F}^{\mathbf{t}} + \mathbf{F}^{\mathbf{r}}). \tag{16}$$

The force and torque imbalance associated with surface tractions is therefore fully solved. The governing equations for the modified boundary problem have the form

$$\left.\begin{aligned} \nabla \cdot \hat{\boldsymbol{\sigma}} + \hat{\mathbf{F}} &= 0 \\ \hat{\boldsymbol{\sigma}} &= \mathbf{C} : \hat{\epsilon} \\ \hat{\epsilon} &= \frac{1}{2}(\nabla \hat{\mathbf{u}} + (\nabla \hat{\mathbf{u}})^{T}) \end{aligned}\right\} \text{in } V, \tag{17}$$

where

$$\hat{\boldsymbol{\sigma}} \cdot \mathbf{n} = \hat{\mathbf{T}} \text{ on } S_T. \tag{18}$$

The superposition method is based on the linear elasticity approximation. The equations are general, in the sense that one can choose any coordinate system. For our convenience, we adopted the Cartesian coordinate system, but there is no restriction on the geometry of a sample, provided that the surface boundary condition is properly defined.

2.2. Finite element method

We used CAST3M [53] to solve the modified boundary problem numerically using FEM [45–47]. A mesh was created corresponding to the sample geometry. Cubic elements with quadratic shape functions and seven integration points were used. Quadratic shape functions are necessary since we need to compute the gradient of strain, which is proportional to the gradient of the shape function. In linear elasticity, the stiffness matrix can be computed using an established FEM procedure [54]:

$$K_{ij} = a(\phi_i, \phi_j), \tag{19}$$

where $\{\phi_i\}_{i \leqslant n}$ is the set of shape functions associated with the n degrees of freedom and a is the bilinear, symmetric and continuous form associated with the elasticity problem.

Using the tractions defined for the modified boundary condition, together with forces due to the corrections for rotation and translation motions, one can formally write

$$\mathbf{K}\hat{\mathbf{u}} = \mathbf{F}^{\mathbf{l}} + \mathbf{F}^{\mathbf{f}}, \tag{20}$$

where $\mathbf{K}$ is the stiffness matrix, $\hat{\mathbf{u}}$ is the displacement field, and $\mathbf{F}^{\mathbf{l}}$ is the external loading due to traction $\hat{\mathbf{T}}$. By solving the above equation one can find the displacement field $\hat{\mathbf{u}}$. Strain field $\hat{\epsilon}$, stress field $\hat{\boldsymbol{\sigma}}$, and the derivative of strain field can then be computed from the field of displacements. We should note that equation (20) only works for a stationary system that exhibits no translational and rotational motion.

In practice, we still have to fix six degrees of freedom in the FEM calculations to guarantee numerical stability. We set the displacements of the centre of mass to zero, and the y and z direction displacements of a very nearby point in its x direction to zero, and the z direction displacement of another very nearby point in its y direction to zero. It is because if the net force and torque of the whole system are zeros, the net force and torque at the centre of mass

are zeros. We have verified this implementation and found that our force-balancing solution in section 2.1 meant that no stress concentration formed near those points.

In fact, if we are only interested in the strain and stress field, and if an FEM solver can handle the dynamic equation

$$\mathbf{M}\ddot{\hat{\mathbf{u}}} + \mathbf{K}\hat{\mathbf{u}} = \mathbf{F}^{\mathbf{l}}, \tag{21}$$

the introduction of the fictitious body $\mathbf{F}^{\mathbf{f}}$ is unnecessary. It is because the strain and stress field are invariant with respect to the rigid body motion. Our treatment in section 2.1 is practically equivalent to putting $\mathbf{F}^{\mathbf{f}} = -\mathbf{M}\ddot{\hat{\mathbf{u}}}$. Similarly, if one can solve the strain field $\hat{\boldsymbol{\epsilon}}$ and stress field $\hat{\boldsymbol{\sigma}}$ directly from traction $\hat{\mathbf{T}}$, without going through the calculation of displacement field $\hat{\mathbf{u}}$, the introduction of $\mathbf{F}^{\mathbf{f}}$ is unnecessary, either.

2.3. Langevin dynamics of defects

Langevin dynamics treatment of defects, including elastic interaction between them, was proposed by Dudarev *et al* [33]. They showed that simulations treating nanoscale radiation defects as elastically interacting objects, with appropriately chosen mobility parameters, can match the real-time dynamics of defects observed in *in-situ* TEM experiments. The Langevin equation of motion for a dislocation loop in the overdamped limit can be written as [33]:

$$\frac{\mathrm{d}w_n}{\mathrm{d}t} = -\frac{D_n}{k_\mathrm{B}T}\frac{\partial E_\mathrm{el}}{\partial w_n} + \sqrt{2D_n}\xi_n(t), \tag{22}$$

where w_n is the position of loop n along the direction of its Burgers vector $\mathbf{b}$, D_n is its diffusion constant, and ξ_n is a randomly fluctuating field satisfying conditions $\langle\xi_n(t)\rangle = 0$ and $\langle\xi_n(t)\xi_n(t')\rangle = \delta(t-t')$. A stochastic force is introduced to take care of the thermally driven diffusivity according to the fluctuation-dissipation theorem [55, 56]. In this work we assume that a glissile loop only moves along the direction defined by its Burgers vector. We do not consider climb or self-climb [57, 58].

Calculating the elastic energy of the system by means of a volume integral

$$E_\mathrm{el} = \frac{1}{2}\int \sigma_{ij}(\mathbf{r})\epsilon_{ij}(\mathbf{r})\mathrm{d}^3 r \tag{23}$$

is time consuming and inefficient. Analytical expressions have been derived for the pairwise elastic interaction between dislocation loops [33, 59], or loops and voids [60] in isotropic elasticity, and these have been used in previous dynamic simulations where loop Burgers vectors were assumed to remain normal to the loop habit planes [23, 33]. This approximation, according to Li *et al* [61], has a relatively limited range of validity, as it neglects the elastic torque acting on a loop, which alters the orientation of its habit plane.

A general way of treating long-range elastic interaction between arbitrary defects, including dislocation loops, is the elastic dipole tensor and Green's function formalism [4, 36–40, 43]. For a given configuration of a defect, its elastic dipole tensor P_{ij} fully defines its long-range elastic field, as discussed below. It also fully defines strain and stress, and hence can be used for finding the elastic energy contribution due to the strains induced by surfaces or applied external stresses. The dipole tensor formalism has been used earlier to bias the movement of defects in kinetic Monte Carlo simulations in an infinite medium [62, 63], but to our knowledge has not been applied to the treatment of surface-induced strains explored below.

The energy of elastic interaction between defects in a finite size sample can be written as a sum of two contributions,

$$E_\mathrm{el} = E_\mathrm{pair} + E_\mathrm{B}. \tag{24}$$

The pairwise part is the energy of elastic interaction between all the defects n and m is [4],

$$E_{\text{pair}} = \frac{1}{2}\sum_{n,m} P^n_{ij} P^m_{kl} G_{ik,jl}(\mathbf{R}^{nm}), \tag{25}$$

where $G_{ik,jl}(\mathbf{R}) = \frac{\partial}{\partial x_j}\frac{\partial}{\partial x_l} G_{ik}(\mathbf{R})$ is the second derivative of elastic Green's function, $\mathbf{R}^{mn} = \mathbf{R}^n - \mathbf{R}^m$ is the directional vector from defect m to n, and the P^n_{ij} is the elastic dipole tensor of defect n. At this level of approximation, elements of elastic dipole tensors are treated as constant parameters characterising the defects, and internal degrees of freedom of defects, treated as point objects, are assumed to be independent of the action of external elastic field.

The second term is due to the modified boundary conditions. The elastic interaction energy between a defect and strain field $\hat{\epsilon}_{ij}$ arising from the modified boundary condition, including the constraining distributed body force, is

$$E_{\text{B}} = -\sum_n P^n_{ij} \hat{\epsilon}_{ij}(\mathbf{R}^n). \tag{26}$$

This can be calculated using FEM for the modified traction condition on S_T and taking into account the fictitious body force, such that:

$$\hat{\mathbf{T}} = -\tilde{\mathbf{T}}, \tag{27}$$

$$\hat{\mathbf{F}} = \mathbf{F}^{\mathbf{f}}, \tag{28}$$

$$\tilde{\mathbf{T}} = \tilde{\boldsymbol{\sigma}} \cdot \mathbf{n}, \tag{29}$$

$$\tilde{\boldsymbol{\sigma}} = \mathbf{C} : \tilde{\boldsymbol{\epsilon}}, \tag{30}$$

where:

$$\tilde{\epsilon}_{ij} = -\sum_n P^n_{kl} G_{ik,jl}(\mathbf{R} - \mathbf{R}_n). \tag{31}$$

This completes the calculation of elastic energy E_{el} for an ensemble of defects in a finite size sample, including effects of elastic interaction with the surface of the sample.

The remaining part of the analysis involves calculating the derivatives of E_{el}. For any mobile defect n, we need to find

$$\frac{\partial E_{\text{el}}}{\partial w_n} = P^n_{ij}\left(\sum_m P^m_{kl}\frac{\partial G_{ik,jl}(\mathbf{R}^{nm})}{\partial w_n} - \frac{\partial \hat{\epsilon}_{ij}(\mathbf{R}^n)}{\partial w_n}\right). \tag{32}$$

The two derivatives with respect to w_n can be evaluated numerically using finite differences. In section 3.2, we present an example of an ensemble of loops in a finite simulation volume. We find 80% of computation time is spent on the FEM calculation for the second term in equation (32).

For an arbitrary material, the evaluation of anisotropic elastic Green's function and its first and second derivative can be performed numerically according to the formula derived by Barnett [64], provided that the elastic constant tensor C_{ijkl} is known. For an arbitrary defect, one can compute P_{ij} from *ab initio* or molecular static calculations [4, 36–43]. Therefore, the formulae in this and the previous section can be applied to any material or defects with no modification.

For a dislocation loop, there is an analytical expression for P_{ij} valid in the linear elasticity limit [4, 34, 59, 65], namely

$$P_{ij} = C_{ijkl} b_k A_l, \tag{33}$$

where b_k and A_l are the Cartesian components of the Burgers vector **b** and the loop vector area **A**. The latter can be expressed as a contour integral over the perimeter of the loop [66]:

$$\mathbf{A} = \frac{1}{2}\oint(\mathbf{r} \times \mathrm{d}\mathbf{l}). \tag{34}$$

Note that **b** and **A** need not to be parallel.

From the elements of elastic dipole tensor, one can also compute the relaxation volume tensor of a defect Ω_{ij} [67], which is a quantity describing swelling of reactor components under irradiation [3]. The relaxation volume tensor is related to the dipole tensor through the elastic compliance tensor $\mathbf{S} = \mathbf{C}^{-1}$, such that [4, 34, 40]

$$\Omega_{ij} = S_{ijkl}P_{kl}. \tag{35}$$

The relaxation volume of a defect equals the trace of the relaxation volume tensor

$$\Omega_{\mathrm{rel}} = \Omega_{11} + \Omega_{22} + \Omega_{33}. \tag{36}$$

We note that the relaxation volume of a dislocation loop, according to equation (33) is simply $\Omega_{\mathrm{rel}} = \mathbf{b} \cdot \mathbf{A}$ irrespective of the elastic properties of a material, and that this equals ± 1 times the total volume of atoms forming the loop (the choice of the sign is positive or negative for an interstitial or vacancy loop, respectively).

The model presented above is based on the elastic dipole tensor and elastic Green's function formalism, and so is valid within the anisotropic linear elasticity approximation. The values for the anisotropic elastic Green's function, and its first and second derivatives can be obtained numerically given the matrix elements of the elastic constant tensor C_{ijkl} [64]. On the other hand, it is not uncommon to treat materials in the isotropic limit, and for the purposes of exposition this limit can offer additional analytical formulae. In the application section, we present examples with parameters for isotropic elasticity only. We should note that the limitation on our numerical implementation does not affect the validity of equations written in terms of anisotropic elasticity.

In the isotropic elasticity case, the elastic constant tensor can be written as [68],

$$C_{ijkl} = \mu\frac{2\nu}{1-2\nu}\delta_{ij}\delta_{kl} + \mu\left(\delta_{ik}\delta_{jl} + \delta_{il}\delta_{jk}\right), \tag{37}$$

where ν is the Poisson ratio and μ is the shear modulus. The elastic Green's function in the isotropic limit is [68]:

$$G_{ik}(\mathbf{r}) = \frac{1}{16\pi\mu(1-\nu)r}\left[(3-4\nu)\delta_{ik} + \frac{x_i x_k}{r^2}\right], \tag{38}$$

and the second derivative of the elastic Green's function is

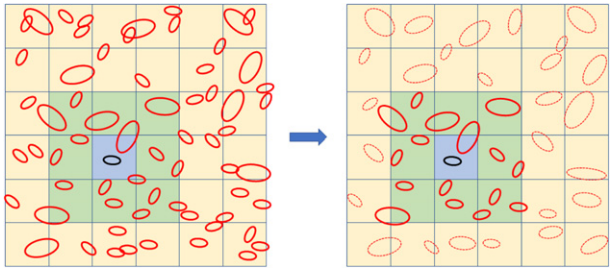

Figure 2. The sample is divided into many regions and the treatment of evolution is implemented using a linked-cell structure. For loops within the same cell and in its neighbouring cells, we compute the exact pairwise interaction between defects. For other interactions, we adopted a coarse-grain method, replacing individual defects within a cell with a single virtual defect according to equations (40) and (41).

$$
\begin{aligned}
G_{ik,jl}(\mathbf{r}) = & \frac{1}{16\pi\mu(1-\nu)r^3} \\
& \times \left[(3-4\nu)\delta_{ik}\left(3\eta_l\eta_j - \delta_{lj}\right) + 15\eta_i\eta_j\eta_k\eta_l \right. \\
& - 3(\delta_{ij}\eta_k\eta_l + \delta_{il}\eta_j\eta_k + \delta_{jl}\eta_i\eta_k + \delta_{kj}\eta_i\eta_l + \delta_{kl}\eta_i\eta_j) \\
& \left. + (\delta_{il}\delta_{kj} + \delta_{ij}\delta_{kl})\right], \qquad (39)
\end{aligned}
$$

where η_i is a component of the radial unit vector $\boldsymbol{\eta} = \mathbf{r}/r$.

2.4. Coarse-grained method and its optimization

In this section we describe an efficient numerical implementation of defect dynamics based on the equations introduced in the previous sections. Firstly, we divided the simulation box into many small regions and adopted a linked-cell structure similar to that used in molecular dynamics codes [69]. A defect is put in a linked list corresponding to the cell containing a defect. The linked lists are updated every time step. The total elastic energy and the integration of equations of motion for mobile defects was performed in parallel using a domain decomposition of the cells. Calculation of strain due to the boundary is also calculated in parallel using the MPI implementation in CAST3M.

Through the linked-cell structure, we can adopt a coarse-grained method to evaluate elastic long-range interaction between defects. For a group of defects at large distances, one can approximate it as a single defect represented by a single dipole tensor, as illustrated in figure 2. According to reference [3], one can approximate the combined far-field effects of the dipole tensor of all defects in a linked cell α using a single virtual defect with dipole tensor

$$
P_{ij}^{\alpha} = \sum_{m\in\alpha} P_{ij}^{m} \qquad (40)
$$

situated at

$$
\mathbf{R}^{\alpha} = \frac{\sum_{m\in\alpha}\|\mathbf{P}^m\|\mathbf{R}^m}{\sum_{m\in\alpha}\|\mathbf{P}^m\|}, \qquad (41)
$$

where $\|\mathbf{P}\| = \sqrt{\mathrm{Tr}(\mathbf{P}^2)}$ is the Frobenius norm.

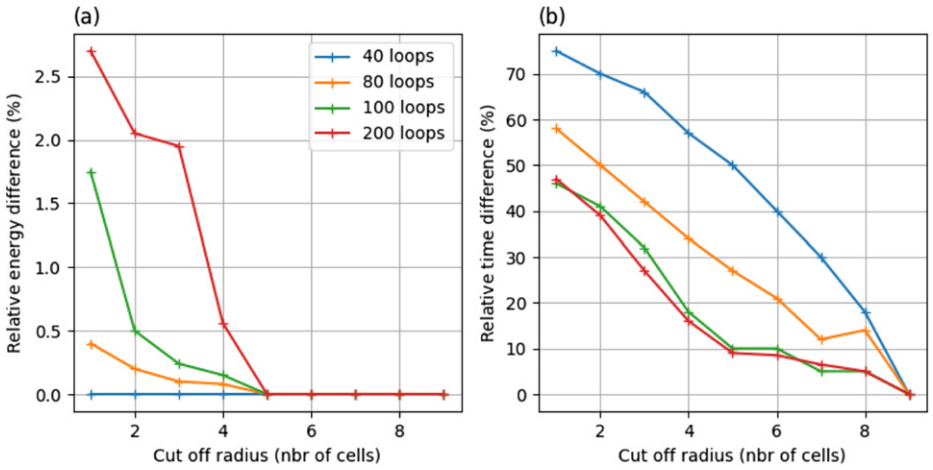

Figure 3. Illustration of a test of the coarse-grained method. We put 40 to 200 loops randomly in a sample of 1 μm $\times$ 1 μm $\times$ 1 μm, where the dimension of each linked cell was 0.1 μm $\times$ 0.1 μm $\times$ 0.1 μm. The cutoff range is the layer of neighbour cells where we still consider full interaction between defects without approximation. (a) The relative energy difference and (b) the relative computation time using different cutoff range.

We verify this approximation using a simulation cell of 1 μm $\times$ 1 μm $\times$ 1 μm, where the dimension of each linked cell is 0.1 μm $\times$ 0.1 μm $\times$ 0.1 μm. We created 40 to 200 loops with random sizes and Burgers vectors inside the sample. Then, we calculate the difference between the total elastic energy of the system with and without this approximation using different cutoff ranges. The cutoff range is the layer of neighbour cells where we still consider full interaction between defects without approximation. For example, if we set the cutoff range at $R_{\text{cut}} = 1$, then all elastic interactions between defects within the same linked cell and its nearest neighbouring cells are considered without approximation, where all the defects starting from the second layer of neighbour cells are approximated using equations (40) and (41).

Figure 3 shows the difference of elastic energy. Even if we consider the cutoff at the first neighbouring cells, the difference is only 3% in a simulation involving 200 loops, yet we achieve double the speed of computation. In figure 4, the values of $\partial E_{\text{el}}/\partial w_n$ for 200 loops calculated using the coarse-grained method with a cutoff distance at the first nearest neighbour cell (meaning interactions outside the first nearest neighbour cell are calculated using the coarse-grained method) are plotted against values calculated without using the coarse-grained method (the limit of large cutoff). We can only see small deviations, and no systematic bias. Since the dynamics of loops depends on the equation of motion, which depends on $\partial E_{\text{el}}/\partial w_n$, in current study, the coarse grained method should have little effect on the dynamics, and thus little effect on the final microstructures. The validity of such an approximation is related to the size of the linked cell, the number of defects in a cell, and the cutoff range. A similar benchmarking test should be performed in any future simulation.

Another interesting observation about the computing time is that, in the limit where the system contains $>$100 loops, for the calculation of defect–defect interaction, about 99% of our computation time is spent on the calculation of elastic interactions within the cutoff range, even when $R_{\text{cut}} = 1$. This indicates that no further coarse-graining is required.

To further speed up simulations, we implemented a simple adaptive time step method. The idea is to have a fast time lapse when nothing interesting happens. For example, if the defects

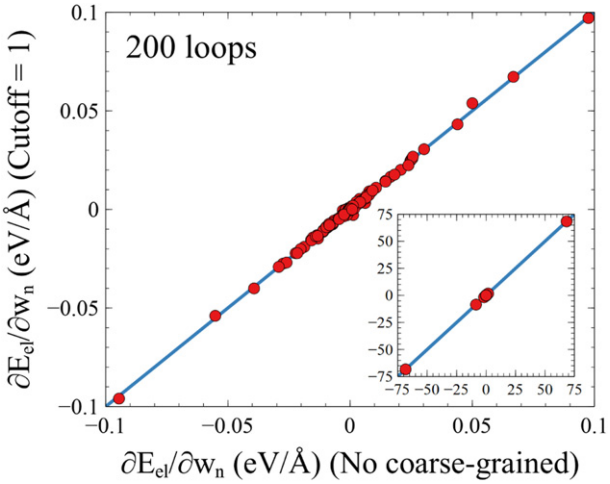

Figure 4. The values of $\partial E_{\mathrm{el}}/\partial w_n$ of 200 loops calculated without using the coarse-grained method are plotted against the values calculated using coarse-grained method with cutoff distance at the first nearest neighbour cell, which means interactions outside the first nearest neighbour cell are calculated using the coarse-grained method.

do not move rapidly, we increase the time step Δt. On the other hand, if a lot of defects are interacting and reacting, we use a smaller Δt. We calculate the displacement of each defect for every 20 time steps. If the maximum displacement for 20 time steps is larger or smaller than 200 Å, we reduce or increase the time step, respectively. In section 3.1, we show that when two loops come close to each other, the elastic interaction energy drops and behaves like an energy well. For tungsten and iron, the characteristic length scale of the energy well is in the order of 100 Å. Therefore, if we consider a displacement within a time step being in the order of 10 Å, it should well describe the dynamics of loops due to the interactions among them. Our implementation leads to a speed up of about five times.

2.5. Parameters and additional rules

The theoretical treatment that we have been discussing so far applies to any material within the linear elasticity approximation, for both isotropic and anisotropic cases. To complete our model, extra rules governing defect interactions that are material and experimental conditions dependent are required. We base our rules on those typically used in okMC simulations [25–31]. The exact parameterisation for a material in the conditions of interest is the subject of ongoing research, but our purpose of this work is to demonstrate the feasibility of our model. Adjustment may be imposed to suit particular material and experimental conditions. We summarize these rules and their rationale below.

We adopt parameters and rules for tungsten in our numerical implementation due to its technological importance in fusion energy. Tungsten has the highest melting point of all the pure metals, as well as high thermal conductivity and low thermal expansion, which makes it ideal for a variety of high heat load applications. Tungsten also has a low physical sputtering yield [70], and its unstable isotopes exhibit relatively fast radioactive decay following neutron irradiation [71]. Presently, tungsten is the preferred candidate material for plasma facing and armour components of the DEMO fusion power plant [72–74].

Experimentally, tungsten is observed to be nearly elastically isotropic, and so we can treat it in our model as isotropic, with Poisson ration $\nu = 0.278$ and shear modulus $\mu = 160$ GPa [75]. All the simulations are performed at room temperature (300 K).

Since high energy neutron irradiation facilities are not widely available, self-ion irradiation experiments are often used for mimicking the effects of high energy neutron irradiation. TEM analysis suggests that vacancy type $\frac{1}{2}\langle 111\rangle$ dislocation loops dominate the *visible* defect populations formed in thin films at low dose $\sim$0.01 dpa [12, 76–80]. For doses in the interval from 0.4 to 30 dpa, the microstructure involves a dense network of line dislocations, finely dispersed vacancies, and interstitial $\frac{1}{2}\langle 111\rangle$ loops [13]. $\langle 100\rangle$ interstitial loops are also observed [81]. These loops are believed to nucleate in collision cascades [8].

Mason *et al* [23], Yi *et al* [78] and Yi *et al* [79] investigated *in-situ* TEM experiments on ultra high purity tungsten foil after self-ion irradiation showing that only dislocation loops with Burgers vector of $\frac{1}{2}\langle 111\rangle$ and $\langle 100\rangle$ were observed. At low dose, vacancy $\frac{1}{2}\langle 111\rangle$ are dominant. When irradiation temperature and dose increase, the fraction of interstitial $\frac{1}{2}\langle 111\rangle$ loops increases. Therefore, we only consider interstitial and vacancy loops with Burgers vector of $\frac{1}{2}\langle 111\rangle$ and $\langle 100\rangle$. We assume that the Burgers vector and the habit plane normal vector of a loop are collinear and do not change during the simulation.

To determine collisions between defects, we use the simplest model, namely that each defect is assumed to be spherical with radius r. The size of a defect equals the absolute value of the number of extra or missing atoms N that constitute the defect, in the unit of atomic volume $\Omega_0 = a^3/2$. The volume of a loop is $V = \pm N\Omega_0 = \mathbf{b}\cdot\mathbf{A}$, where $\mathbf{b}$ is the Burgers vector, $\mathbf{A}$ is the area vector, and N is the equivalent point defect count in the defect. When the sign is positive (negative), the defect is of interstitial (vacancy) type. The radius of a prismatic loop is defined according to $|\mathbf{A}| = \pi r^2$.

A unique and pioneering experiment using high voltage *in-situ* TEM by Arakawa *et al* [82] showed that when two nanoscale loops in bcc iron collide, a junction is formed between the two loops. Then, the junction would move towards the far end of the smaller loop. Finally, the larger loop absorbs the smaller loop. Our rule for loop coalescence is that when the distance between the two defects is smaller than the sum of their radius, i.e. $d < r_1 + r_2$, the larger defect absorbs the smaller one. When a defect is absorbed by another defect, all the characters of the new defect follow the larger defect. When two defects of the same size combine, the characters of the new defect follow one of the original defects by random. Though we have not found similar experimental works in other bcc metals, we adopt this rule for our simulations on tungsten based on the fact that they have the same crystal structure.

Yi *et al* [79] observed that $\frac{1}{2}\langle 111\rangle$ loops perform one dimensional diffusion in tungsten, where $\langle 100\rangle$ loops are sessile. Arakawa *et al* [83] observed that a nanoscale interstitial $\frac{1}{2}\langle 111\rangle$ loop in bcc iron undergoes one dimensional Brownian type diffusion, which is not driven by external stress. MD simulations show that $\frac{1}{2}\langle 111\rangle$ loops in bcc metals are extremely mobile along their glide cylinders [84, 85]. In our model therefore a $\frac{1}{2}\langle 111\rangle$ loop is moving in one dimension, and performs Brownian motion biased by elastic interactions, and does not rotate, whereas a $\langle 100\rangle$ loop is sessile. When a defect moves away from the simulation box, it is discarded.

The diffusion constant D_n for dislocation loops is assumed to be inversely proportional to the loop area. We take the numerical value for tungsten from Swinburne *et al* [85]:

$$D_n(T,N) = \frac{176\sqrt{85^2+T^2}}{\sqrt{N}}\ \mu\mathrm{m}^2\ \mathrm{s}^{-1}, \tag{42}$$

where T is the absolute temperature expressed in Kelvin units, and N is the number of atoms in a $\frac{1}{2}\langle 111\rangle$ loop.

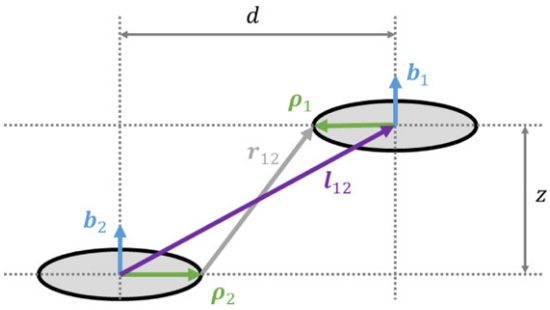

Figure 5. A schematic illustration of a set of two parallel loops.

All the extra rules mentioned here are deterministic. The only stochastic effect due to thermal excitation is incorporated in the over-damped Langevin equation of motion through the fluctuation-dissipation theorem. Selection of parameters and rules may have significant effect on the results, as one can see in different okMC models [25–30, 32] and cluster dynamics models [86, 87]. The main purpose of this work is to demonstrate the feasibility of our defect dynamics model based on the elastic dipole tensor and elastic Green's function. It is not the goal of the present manuscript to determine the effect of a parameter choice or physical interaction rule on the evolution of microstructure. A detailed analysis of such matters is an opportunity for further research.

3. Applications

3.1. Two loops with parallel Burgers vectors

In the first example we verify the validity of the dipole tensor and Green's function formalism, and compare it with the analytical expression from the linear elasticity theory [33, 75]. We put two loops with parallel Burgers vectors in an infinite medium. A schematic illustration is shown in figure 5. They are elastically interacting and undergo Brownian motion. We observe their displacements and compare our results with the work by Dudarev *et al* [33]. This also allows us to prove the correctness of the implementation of our formula and algorithms. For clarity of exposition, we do not consider surface effects here. The elastic contribution due to surfaces will be examined below.

Parameters for iron and tungsten in the isotropic elasticity approximation are chosen for demonstration. The Poisson ration $\nu = 0.291$ and shear modulus $\mu = 86$ GPa for iron, and $\nu = 0.278$ and $\mu = 160$ GPa for tungsten [75]. Two interstitial $\frac{1}{2}\langle 111\rangle$ dislocation loops are put side by side with a horizontal separation of $d = 37$ nm. One loop has a diameter of 16 nm and the other has a diameter of 15 nm. The diffusion constants for the loops in the case of iron are taken as $D_1 = 296\ \mathrm{nm}^2\ \mathrm{s}^{-1}$ and $D_2 = 315\ \mathrm{nm}^2\ \mathrm{s}^{-1}$, respectively. We take the same parameters and configurations for iron as in reference [33] for direct comparison. In the tungsten case, the diffusivity of loops is taken according to equation (42), where $D_1 = 929\ \mu\mathrm{m}^2\ \mathrm{s}^{-1}$ and $D_2 = 991\ \mu\mathrm{m}^2\ \mathrm{s}^{-1}$.

Dynamic simulations are performed according equation (22). Figure 6 shows the displacements of the two loops as functions of time for iron and tungsten. In both cases, the two loops perform correlated motion. This can be understood by inspecting the elastic interaction energy between two loops.

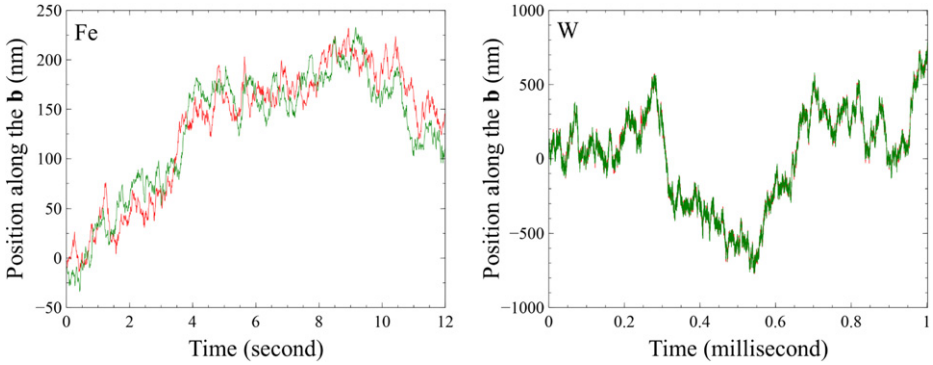

Figure 6. Dynamic evolution of positions of two loops in iron and tungsten. One loop has a diameter of 15 nm and the other has a diameter of 16 nm. Their horizontal separation $d = 37$ nm. Loop move in the direction of their Burgers vectors.

The energy of two interacting circular loops with parallel Burgers vector $\mathbf{b}_1$ and $\mathbf{b}_2$ in the isotropic limit, according to Hirth and Lothe, can be written as [33, 75]:

$$U_{\mathrm{HL}} = \frac{\mu b_1 b_2}{4\pi(1-\nu)} \int_0^{2\pi} \mathrm{d}\phi_1 \int_0^{2\pi} \mathrm{d}\phi_2 \left\{ \frac{\boldsymbol{\rho}_1(\phi_1) \cdot \boldsymbol{\rho}_2(\phi_2)}{r_{12}} - \frac{(\mathbf{r}_{12} \cdot \boldsymbol{\rho}_1(\phi_1))(\mathbf{r}_{12} \cdot \boldsymbol{\rho}_2(\phi_2))}{r_{12}^3} \right\}, \tag{43}$$

where $\mathbf{r}_{12} = \mathbf{l}_{12} + \boldsymbol{\rho}_1 - \boldsymbol{\rho}_2$ is a vector from a point on the perimeter of a loop to a point on the perimeter of the other loop, $\mathbf{l}_{12}$ is the vector from the centre of one loop to the centre of the other, and $\boldsymbol{\rho}_1$ and $\boldsymbol{\rho}_2$ are the radial vectors in the habit plane of the loops.

Alternatively, in terms of the dipole tensor and elastic Green's function, the elastic energy between the two loops can be written as (see equation (25)):

$$U_{\mathrm{Green}} = P^1_{ij} G_{ik,jl}(\mathbf{l}_{12}) P^2_{kl}, \tag{44}$$

where P^1_{ij} and P^2_{kl} are dipole tensors of loops 1 and 2. It is expected that equation (44) gives the same value as equation (43) when the two loops are separated by a distance several times their radius, consistent with the far field approximation. However, equation (44) is a more general formula using which one can treat any interacting defects provided that their dipole tensors are known.

Figure 7 shows U_{HL} and U_{Green} for two circular interstitial loops with Burgers vectors pointing in the same $\frac{1}{2}\langle 111\rangle$ direction. Each loop contains 55 extra atoms. The horizontal distance between the centre of the two glide cylinders is $d = 41$ Å. The elastic energy of loops is plotted against the difference between positions of the loops in the direction of their collinear Burgers vectors.

We can see there is a clear energy well in both iron and tungsten. This is why two dislocation loops diffuse in correlated motion as observed experimentally and explained theoretically [33]. The numerical values of U_{Green} is almost the same as U_{HL} when the two loops are far apart. When they come closer, the numerical value of U_{HL} and U_{Green} are not identical, but the shape of the well remains the same. This means that the direction of forces remains the same, even if their magnitudes are slightly different. When the vertical distance between two loops is within the energy well, the two loops are trapped by each other and perform correlated diffusion [33].

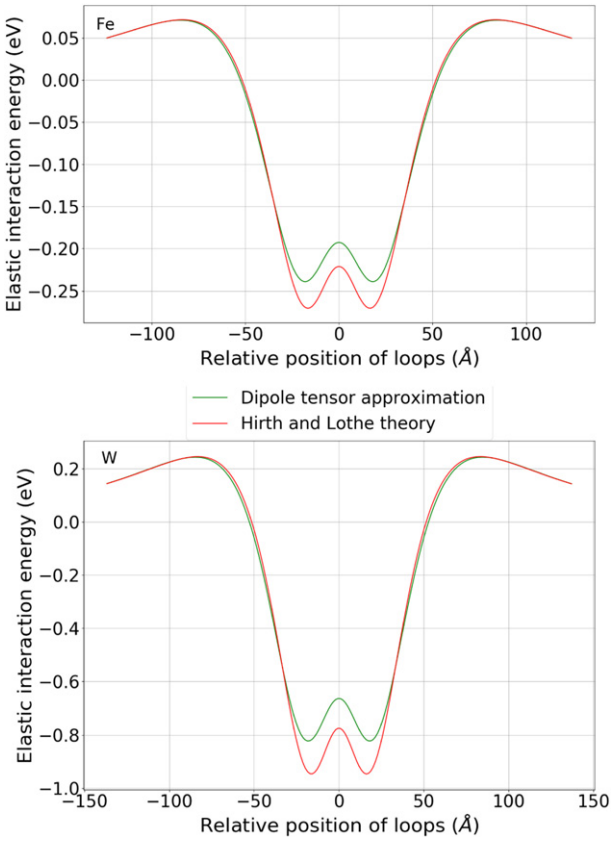

Figure 7. The elastic energy of interaction between two loops in iron and tungsten with parallel Burgers vectors plotted against their vertical separation z. Each loop contains 55 atoms. The horizontal distance between the centre of the two glide cylinders is $d = 41$ Å.

The difference in U_{HL} and U_{Green} when two loops come close is due to the use of the far field approximation in U_{Green}. The value of U_{HL} is obtained through double integration around the perimeters of the two loops, summing the elastic interaction between infinitesimal line segments of each loop. The elastic dipole tensor describes a defect as a point object, so U_{Green} is less accurate when two loops are close. Nevertheless, the functional form of U_{Green} allows one to treat all sort of defects in different orientations, and is not limited to parallel dislocation loops.

The energy well is deeper in the tungsten case than in the iron case, which means the elastic forces in tungsten case are stronger when two loops are close. Since both the force on and diffusivity of loops in tungsten case are much larger, a smaller time-step is required to calculate the displacement of loops in tungsten case with good numerical stability. This is the origin of the smaller time scale in the case of tungsten in figure 6.

We can calculate the observed diffusivity of each loop and also the diffusivity of the centre of mass of the two loops. The observed diffusivity is calculated according to

$$D_i^{\mathrm{obs}} = \sum_{t=0}^{N} \frac{|w_i(t+1) - w_i(t)|^2}{2N\Delta t}, \tag{45}$$

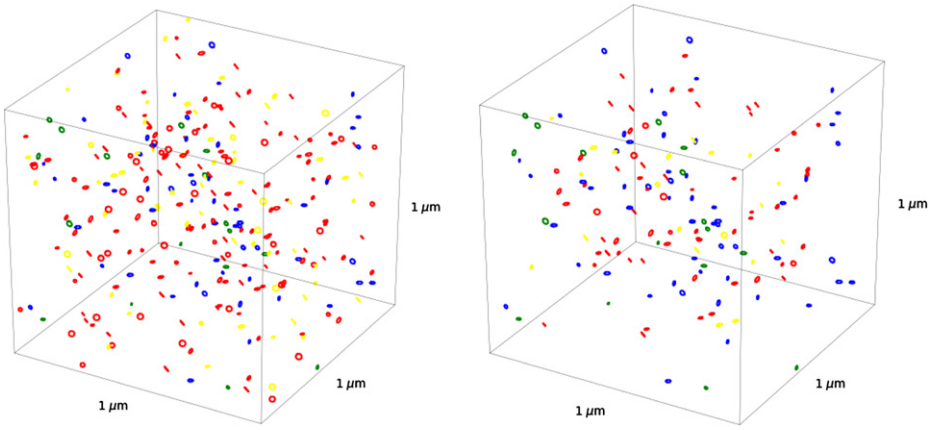

Figure 8. (Left) The initial configuration of a sample containing 300 dislocation loops at 300 K. (Right) The configuration of a sample at time $t = 3.0 \times 10^{-6}$ s. Sessile SIA loops are shown in blue. Glissile SIA loops are shown in red. Sessile vacancy loops are shown in green. Glissile vacancy loops are shown in yellow.

where $w_i(t)$ is the position of a loop i at time t. The diffusivity of the set of two loops can be calculated using the same formula, but replacing the $w_i(t)$ by $W(t)$, which is the position of the centre of mass.

According to reference [33], the diffusion-weighted centre of position of loops is

$$W(t) = (D_1 w_2(t) + D_2 w_1(t))/(D_2 + D_1), \tag{46}$$

and the diffusion coefficient of the system of two loops is

$$\bar{D} = \frac{D_1 D_2}{D_1 + D_2}, \tag{47}$$

where D_i is the diffusion coefficient of loop i in an infinite medium with no interaction with other defects.

We calculated the expected diffusion coefficient $\bar{D}$ using the values of D_1 and D_2 given above, and the observed diffusion coefficient D^{obs} of the centre of position of the two loops using equation (45). We found that in iron, $\bar{D} = 152.6$ nm^2 s^{-1} and $D^{\text{obs}} = 143$ nm^2 s^{-1}, whereas in tungsten, $\bar{D} = 479.5$ μm^2 s^{-1} and $D^{\text{obs}} = 477$ μm^2 s^{-1}. They compare with each other very well. The displacement and timescale in the iron case are compatible with the data by Dudarev *et al* [33]. This confirms the validity of our algorithm and the feasibility of using the elastic dipole tensor and Green's function formalism in practical simulations.

3.2. Dislocation loops in a sample of finite size

In another example, we put a number of loops in a finite size sample. We have adopted parameters and rules for tungsten as discussed in section 2.5. Dislocation loops evolve dynamically, subject to elastic interactions with other loops and also with surfaces. The example involves using coupled Langevin defect dynamics complemented with the FEM scheme. It enables studying the effect of surfaces on the dynamics of defects.

Initially, 300 dislocation loops were positioned randomly inside a box with dimensions of 1 μm $\times$1 μm $\times$1 μm. Loop diameters were chosen uniformly in the range of sizes from 4 nm

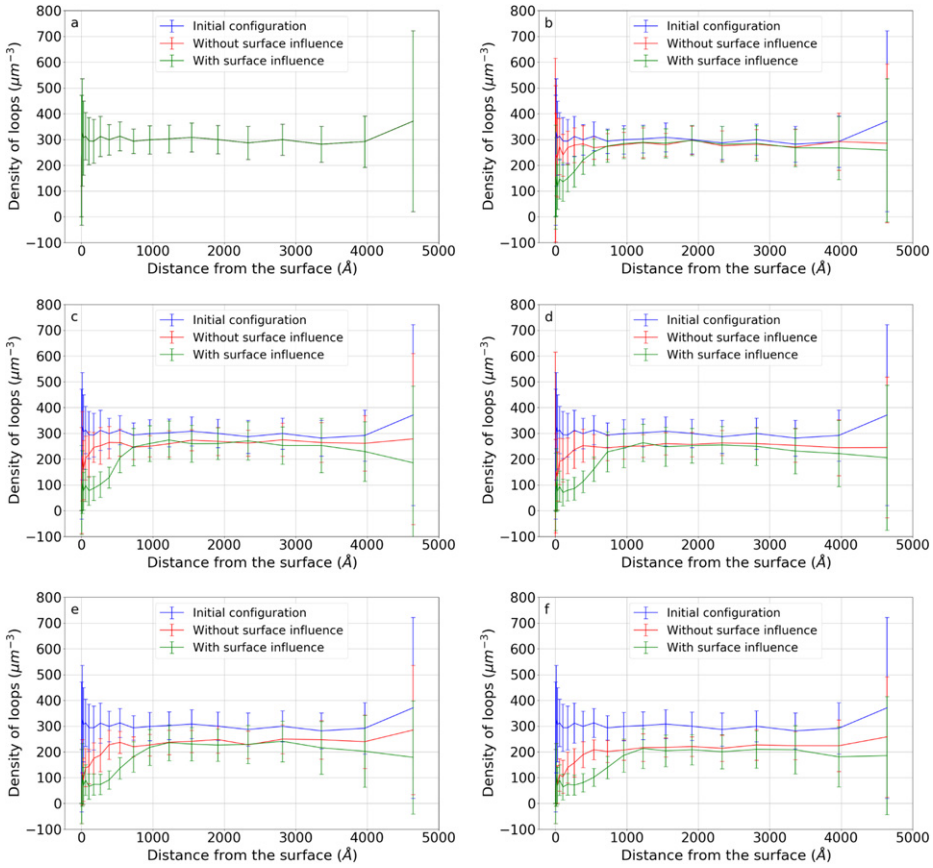

Figure 9. Density of loops with respect to the original number of loops against the depth from the surface. The initial configuration is in blue. The one with surface effects is in green. The one without is in red. All data are calculated as an average of 50 simulations, where the error bars are their standard deviation. From left to right, top to bottom: (a) $t = 0$ s, (b) $t = 1.0 \times 10^{-8}$ s, (c) $t = 5.0 \times 10^{-8}$ s, (d) $t = 1.0 \times 10^{-7}$ s, (e) $t = 5.0 \times 10^{-7}$ s, and (f) $t = 3.0 \times 10^{-6}$ s.

to 11 nm. There are 75% interstitial loops and 25% vacancy loops, where 75% are $\frac{1}{2}\langle 111\rangle$ and 25% are $\langle 100\rangle$ loops. Burgers vector of a loop is assigned randomly to all the crystallographically equivalent directions. These parameters are taken roughly similar to loops nature and number density observed in self-ion irradiated TEM experiments [12, 77–79]. They are generated and put randomly in the sample in a uniform distribution, as illustrated in figure 8.

We performed simulations with and without coupling to FEM, that is with and without elastic coupling to surfaces. We created 50 different initial configurations as starting points for both studies. All the results are presented as average values, with the error bars giving the sample standard deviation. In both cases, we expect that the density of loops vanishes at the surface after a long period of time, as surfaces acts as sinks for defects.

Figure 9 shows the time evolution of the density of loops with respect to the original number of loops against distance to the surface. The sample is divided into cubic shells contained within each other. Each data point is calculated within the region of an onion-like shell. The distance of a defect from the surface is calculated according to its minimum distance to the surface. In

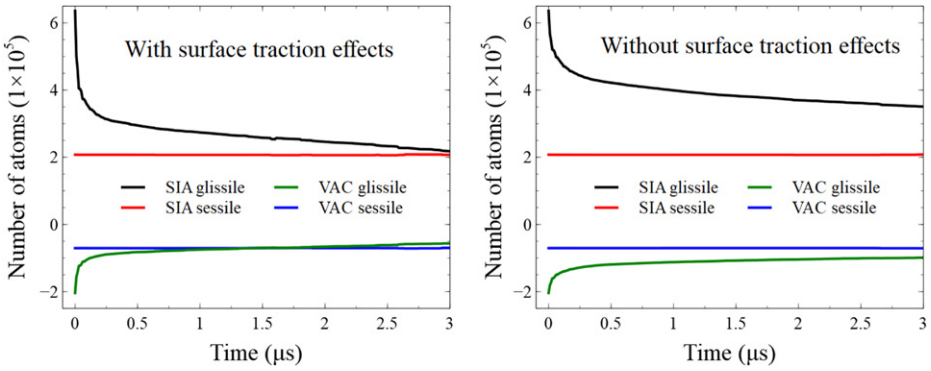

Figure 10. The total number of constituent atoms being involved in different kinds of loops with and without surface traction effects through FEM.

order to keep the volume in each onion-like shell the same, its thickness increases when it is far away from the surface and approaching the centre of the sample.

Initially the density of loops is almost flat at 300 μm^{-3}, which is compatible with the initial condition that 300 loops were put in a 1 μm^3 box. As time progresses, the evolution of the system proceeds differently depending on the boundary conditions. When there is elastic coupling to surfaces, that is in simulations done using FEM, the loop density near the surfaces decreases faster, compared to simulations neglecting the surface effects. In both cases, the loop density stays flat in the bulk-like region. The elastic interaction between the surfaces and the loops drives loops towards the surface, from where they can leave the box. It appears that elastic contribution from the surface enhances the mobility of loops near it, and this effect is felt over tens of nanometres.

Figure 10 shows the total number of constituent point defects in dislocation loops as a function of time. Vacancy loops correspond to negative values. For both SIA and vacancy sessile loops, their values are generally decreasing, through coalescence and recombination with glissile loops. However, their changes are small compared to glissile loops, and hardly discernible in figure 10. This result is a consequence of the initial homogeneous distribution of defects. If we instead use highly correlated initial positions, for example using the spatially varying density of defects observed in MD and experiment [88], we see a very rapid initial period of defect recombination strongly dependent on the specific rules used to generate the defect distribution and to determine defect collisions. Correctly constructing a set of quasi-independent defects from cascade collapse is an ongoing area of research [63]. As this paper is concerned with proving an efficient computational scheme for the evolution of quasi-independent defects, explicit cascade relaxation simulations are outside our present scope.

Comparing the cases with and without surface traction effects, through with or without coupling to FEM, the decrease on the total number of constituent atoms of SIA glissile loops and increase in vacancy glissile loops is more significant in the case with FEM. This is consistent with figure 9. A glissile loop away from the centre of the simulation cell is attracted elastically by its image forces, and this causes glissile loops to escape more easily from the box. We can see a surface depletion layer when compared to the initial configuration. Figure 8 also illustrates a configuration simulated with FEM at time $t = 3.0 \times 10^{-6}$ s.

Figure 11 shows the change of the average relaxation volume with and without surface tractions. We initially put more interstitial loops in the box, so the initial relaxation volume is positive. The relaxation volume drops in both cases because glissile loops escape from the

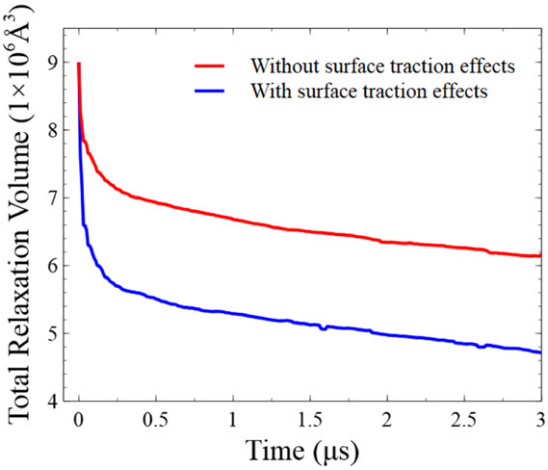

Figure 11. Average relaxation volume in samples containing initially 300 dislocations loops versus time.

simulation cell. We can also see those simulated with surface tractions have a lower relaxation volume at finite times, again due to the enhanced glissile loop loss.

4. Discussion and outlook

A full simulation on an *in-situ* ion or neutron irradiation TEM experiments is very involved. One needs to consider many other aspects beyond the scope of this work. Nevertheless, we may discuss some of them as part of possible extension of current model.

The most significant rule we have not incorporated is the pinning of loops by carbon impurities. It has been known to be a very significant factor in determining the effective diffusion constant of mobile interstitial defects [89–91]. Carbon will slow, or even stop dislocation loops depending on the binding energy, which may be as high as 2 eV [92]. In neglecting the retarding effect of carbon, we are looking at the most challenging case from a computational perspective, with all defects having maximum mobility.

In addition to dislocation loops, one could consider interstitial atom, vacancy, and void within the formalism presented here. Frenkel pairs are generated continuously in collision cascades. Voids can be formed through the agglomeration of vacancies, or through thermal transformation from vacancy loops. Gilbert *et al* [93] using molecular statics showed that prismatic $\frac{1}{2}\langle 111\rangle$ interstitial loop and void are most stable defect structures for interstitial and vacancy type in tungsten, respectively. At high temperature, one may also consider the processes of interstitial ejection or vacancy ejection from defects. The generation of proper size and species distribution of defects due to random collision cascades may be based work by Mason *et al* [23]. Guided by MD simulation [8] and *in situ* TEM experiments [12], we know that the size-frequency distribution of interstitial loops, vacancy loops, and voids should follow power laws. TEM experimental analysis also shows that loops should be spatially distributed with a number density, $\rho(R)$, exponentially decreasing with distance from the centre of the cascade, i.e. $4\pi R^2\rho(R)\mathrm{d}R \sim \exp(-R/\lambda)\mathrm{d}R$ [88], and that individual defects are generated independently [94]. Meeting all three conditions simultaneously requires thought as the total interstitial count must equal the total vacancy count, split between loops and clusters, and touching defects will spontaneously transform.

Self-climb of a dislocation loop is a result of pipe diffusion around the loop perimeter. Atoms diffuse along the dislocation like a short circuit path [57, 58]. This effect could be incorporated by considering stochastic motion perpendicular to the gliding direction. Defect mediated climb changes the size and shape of a loop [57]. Our model can, in principle, incorporate such climb, though this requires okMC-like rules for the combination of small and large defects when they come close enough. Elastic dipole tensor and diffusivity of small mobile defects will be required. Since we are using the elastic dipole tensor formalism, there is arbitrariness on the choice of shape of a loops. Parameterizing such rules will rely on information input from experiments or atomic scale simulations.

In contrast to cluster dynamics, which also describes the evolution of an ensemble of defects, our method considers the real dynamics of defects with spatial resolution. This allows us to consider the elastic interactions among all defects simultaneously by simply integrating the equation of motion, whereas cluster dynamics [86, 87] is based on solving a mean-field rate equation.

The modern okMC method [25–30, 32], using the Bortz–Kalos–Lebowitz (BKL) algorithm [95], is often accelerated using basin-finding algorithms [96, 97]. Elastic interactions may be introduced as a bias on the migration energy [98]. When a model contains a large amount of defects whose migration rates depend on their relative positions, as is the case with elastic interactions, the number of possible exit states from the equilibrating basin becomes very large and the time progression will be slow. A recent development on parallel okMC method [31] bypassed the BKL algorithm. They progress the time through a fixed time step, which is inversely proportional to the maximum event rate. By exploiting the massive parallel power of GPU, they generate random numbers for all possible processes to decide whether a process will happen or not within a time step. However this approach makes it more difficult to correctly incorporate long-range elastic interactions with strict causality. For these reasons okMC works considering the elastic interaction between defects [23, 28, 29, 32, 62, 63, 99] have been restricted to small system size.

The computation efficiency of our code implementation may be further improved. Currently, the code for defect–defect interactions is written in Python. A substantial improvement is expected if it is written in C++ or Fortran. The FEM simulation is performed using CAST3M. In this study, its MPI implementation was limited to only 32 CPU cores in a single computer node. Each time step takes about 3 min, where 80% of computer time is spent on the FEM solver.

5. Conclusion

We have developed a Langevin dynamics model coupled to a FEM that simulates the dynamics of localized defects in a finite size elastic medium, where the interaction between defects is described by the elastic dipole tensor and elastic Green's function formalism. The current model is valid within the linear elasticity approximation. This is appropriate for simulating ion and neutron irradiation experiments where localized defects are generated by collision cascades. We have solved the problem of artificial imbalanced forces and moments that appears in traction free boundary conditions when the superposition method is used. We have demonstrated the validity and feasibility of our model through examples. We performed a dynamic simulation of two interacting loops, that is well compatible with a previous work that used an analytic solution and parallel loops. We have also simulated the dynamics of an ensemble of loops in a finite size box, and observed the elastic contribution due to surfaces. We can see that surfaces enhance the mobility of loops and so act as a strong sink. The density of loops near surface is lower if elastic interaction with surface is considered. We have demonstrated

that our model is capable of simulating time and length scales approaching experimental scales. This model allows us to simulate the evolution of defects that may explain observations from TEM.

Acknowledgments

Federico Baraglia acknowledges financial support from French Embassy in London for his six months internship at Culham Centre for Fusion Energy, UK Atomic Energy Authority. We are grateful to Dr. Edmund Tarleton of the University of Oxford for fruitful discussions about the finite element method. We also thank D R Mason and S L Dudarev of Culham Centre for Fusion Energy for stimulating discussions and critical reviews of this manuscript. This work has been carried out within the framework of the EUROfusion Consortium and has received funding from the Euratom research and training programme 2014–2018 and 2019–2020 under Grant agreement No. 633053 and from the RCUK Energy Programme [Grant No. EP/T012250/1]. To obtain further information on the data and models underlying this paper please contact PublicationsManager@ukaea.uk. The views and opinions expressed herein do not necessarily reflect those of the European Commission. We acknowledge computing resources supplied by the IRIS (STFC) Consortium.

ORCID iDs

Federico Baraglia https://orcid.org/0000-0001-9612-243X
Pui-Wai Ma https://orcid.org/0000-0002-4491-2525

References

[1] Zinkle S J and Busby J T 2009 *Mater. Today* **12** 12–9
[2] Zinkle S J and Was G S 2013 *Acta Mater.* **61** 735–58
[3] Dudarev S L, Mason D R, Tarleton E, Ma P-W and Sand A E 2018 *Nucl. Fusion* **58** 126002
[4] Dudarev S L and Ma P W 2018 *Phys. Rev. Mater.* **2** 033602
[5] Hofmann F *et al* 2015 *Acta Mater.* **89** 352–63
[6] Sato S and Maki K 2003 *Fusion Eng. Des.* **65** 501–24
[7] Gilbert M R, Dudarev S L, Zheng S, Packer L W and Sublet J-C 2012 *Nucl. Fusion* **52** 083019
[8] Sand A E, Dudarev S L and Nordlund K 2013 *Europhys. Lett.* **103** 46003
[9] Sand A E, Nordlund K and Dudarev S L 2014 *J. Nucl. Mater.* **455** 207–11
[10] Sand A E, Aliaga M J, Caturla M J and Nordlund K 2016 *Europhys. Lett.* **115** 36001
[11] Sand A E, Mason D R, De Backer A, Yi X, Dudarev S L and Nordlund K 2017 *Mater. Res. Lett.* **5** 357–63
[12] Yi X, Sand A E, Mason D R, Kirk M A, Roberts S G, Nordlund K and Dudarev S L 2015 *Europhys. Lett.* **110** 36001
[13] Derlet P M and Dudarev S L 2020 *Phys. Rev. Mater.* **4** 023605
[14] Hofmann F, Mason D R, Eliason J K, Maznev A A, Nelson K A and Dudarev S L 2015 *Sci. Rep.* **5** 16042
[15] Cui S, Doerner R P, Simmonds M J, Xu C, Wang Y, Dechaumphai E, Fu E, Tynan G R and Chen R 2018 *J. Nucl. Mater.* **511** 141–7
[16] Reza A, Yu H, Mizohata K and Hofmann F 2019 Thermal diffusivity degradation and point defect density in self-ion implanted tungsten *Acta Mater.* **193** 270–9
[17] Hasegawa A, Fukuda M, Nogami S and Yabuuchi K 2014 *Fusion Eng. Des.* **89** 1568–72
[18] Durrand-Charre M 2003 *Microstructure of Steels and Cast Irons* (Berlin: Springer)
[19] Liu C, He L, Zhai Y, Tyburska-Püschel B, Voyles P M, Sridharan K, Morgan D and Szlufarska I 2017 *Acta Mater.* **125** 377–89

[20] Larson B C 2019 *Crystals* **9** 257
[21] Aliaga M J, Schäublin R, Löffler J F and Caturla M J 2015 *Acta Mater.* **101** 22–30
[22] Sand A E, Byggmästar J, Zitting A and Nordlund K 2018 *J. Nucl. Mater.* **511** 64–74
[23] Mason D R, Yi X, Kirk M A and Dudarev S L 2014 *J. Phys.: Condens. Matter.* **26** 375701
[24] Fikar J, Gröger R and Schäublin R 2017 *Nucl. Instrum. Methods Phys. Res.* B **393** 186–9
[25] Domain C, Becquart C S and Malerba L 2004 *J. Nucl. Mater.* **335** 121–45
[26] Martin-Bragado I, Rivera A, Valles G, Gomez-Selles J L and Caturla M J 2013 *Comput. Phys. Commun.* **184** 2703–10
[27] Castin N, Bakaev A, Bonny G, Sand A E, Malerba L and Terentyev D 2017 *J. Nucl. Mater.* **493** 280–93
[28] Sivak A B, Romanov V A and Chernov V M 2010 *Crystallogr. Rep.* **55** 97–108
[29] Sivak A B, Chernov V M, Romanov V A and Sivak P A 2011 *J. Nucl. Mater.* **417** 1067–70
[30] Caturla M J 2019 *Comput. Mater. Sci.* **156** 452–9
[31] Jiménez F and Ortiz C J 2016 *Comput. Mater. Sci.* **113** 178–86
[32] Mock M, Stein P, Hin C and Albe K 2019 *J. Nucl. Mater.* **527** 151807
[33] Dudarev S L, Gilbert M R, Arakawa K, Mori H, Yao Z, Jenkins M L and Derlet P M 2010 *Phys. Rev.* B **81** 224107
[34] Dederichs P H, Lehmann C, Schober H R, Scholz A and Zeller R 1978 *J. Nucl. Mater.* **69–70** 176–99
[35] Schilling W 1978 *J. Nucl. Mater.* **69–70** 465–89
[36] Clouet E, Garruchet S, Nguyen H, Perez M and Becquart C S 2008 *Acta Mater.* **56** 3450–60
[37] Clouet E, Varvenne C and Jourdan T 2018 *Comput. Mater. Sci.* **147** 49–63
[38] Varvenne C, Bruneval F, Marinica M C and Clouet E 2013 *Phys. Rev.* B **88** 134102
[39] Varvenne C and Clouet E 2017 *Phys. Rev.* B **96** 224103
[40] Ma P W and Dudarev S L 2019 *Phys. Rev. Mater.* **3** 013605
[41] Ma P W and Dudarev S L 2019 *Phys. Rev. Mater.* **3** 043606
[42] Ma P W and Dudarev S L 2019 *Phys. Rev. Mater.* **3** 063601
[43] Ma P W and Dudarev S 2019 *Comput. Phys. Commun.* **252** 107130
[44] Leibfried G and Breuer N 1978 *Point Defects in Metals* (Berlin: Springer)
[45] Belytschko T, Liu W and Moran B 2000 *Nonlinear Finite Elements for Continua and Structures* (New York: Wiley)
[46] Malvern L 1969 *Introduction to the Mechanics of a Continuous Medium* (*Prentice-Hall Series in Engineering of the Physical Sciences*) (Englewood Cliffs, NJ: Prentice-Hall)
[47] Zienkiewicz O, Taylor R and Zhu J 2013 *The Finite Element Method: Its Basis and Fundamentals* 7th edn (Oxford: Butterworth–Heinemann)
[48] van der Giessen E and Needleman A 1995 *Modelling Simul. Mater. Sci. Eng.* **3** 689–735
[49] Verdier M, Fivel M and Groma I 1998 *Modelling Simul. Mater. Sci. Eng.* **6** 755–70
[50] Fivel M C and Canova G R 1999 *Modelling Simul. Mater. Sci. Eng.* **7** 753–68
[51] Weygand D, Friedman L H, van der Giessen E and Needleman A 2002 *Modelling Simul. Mater. Sci. Eng.* **10** 437–68
[52] Bromage B and Tarleton E 2018 *Modelling Simul. Mater. Sci. Eng.* **26** 085007
[53] Combescure A, Hoffmann A and Pasquet P 1982 *The CASTEM Finite Element System* (Berlin: Springer) pp 115–25
[54] Ern A and Guermond J L 2004 *Theory and Practice of Finite Elements* (*Applied Mathematical Sciences*) (New York: Springer)
[55] Chandrasekhar S 1943 *Rev. Mod. Phys.* **15** 1–89
[56] Kubo R 1966 *Rep. Prog. Phys.* **29** 255–84
[57] Swinburne T, Arakawa K, Mori H, Yasuda H, Isshiki M, Mimura K, Uchikoshi M and Dudarev S 2016 *Sci. Rep.* **6** 30596
[58] Liu F, Cocks A C F, Gill S P A and Tarleton E 2020 *Modelling Simul. Mater. Sci. Eng.* **28** 055012
[59] Dudarev S L and Sutton A P 2017 *Acta Mater.* **125** 425–30
[60] Baštecká J and Kroupa F 1964 *Czech. J. Phys.* B **14** 443–53
[61] Li Y, Boleininger M, Robertson C, Dupuy L and Dudarev S L 2019 *Phys. Rev. Mater.* **3** 073805
[62] Subramanian G, Perez D, Uberuaga B, Tomé C and Voter A 2013 *Phys. Rev.* B **87** 144107
[63] Mason D R, Sand A E and Dudarev S L 2019 *Modelling Simul. Mater. Sci. Eng.* **27** 055003
[64] Barnett D M 1972 *Phys. Status Solidi (b)* **49** 741–8
[65] Trinkaus H 1972 *Phys. Status Solidi (b)* **54** 209–18
[66] Landau L D and Lifshits E M 1986 *Theory of Elasticity* 3rd edn (Oxford: Butterworth–Heinemann) p 112

[67] Puchala B, Falk M L and Garikipati K 2008 *Phys. Rev.* B **77** 174116
[68] Mura T 1987 *Micromechanics of Defects in Solids* 2nd edn (Berlin: Springer)
[69] Allen M P and Tildesley D J 1987 *Computer Simulation of Liquids* (*Oxford Science Publications*) (Oxford: Clarendon)
[70] Federici G *et al* 2001 *Nucl. Fusion* **41** 1967
[71] Gilbert M R and Sublet J-C 2011 *Nucl. Fusion* **51** 043005
[72] Donné A J H and Morris W 2018 *European Research Roadmap to the Realisation of Fusion Energy* (EUROfusion) URL http://euro-fusion.org/eurofusion/roadmap
[73] Rieth M *et al* 2011 *J. Nucl. Mater.* **417** 463–7
[74] Rieth M *et al* 2013 *J. Nucl. Mater.* **432** 482–500
[75] Hirth J and Lothe J 1982 *Theory of Dislocations* (Malabar, FL: Krieger) URL https://books.google.co.uk/books?id=LFZGAAAAYAAJ
[76] Jäger W and Wilkens M 1975 *Phys. Status Solidi (a)* **32** 89–100
[77] Yi X, Jenkins M L, Briceno M, Roberts S G, Zhou Z and Kirk M A 2013 *Phil. Mag.* **93** 1715–38
[78] Yi X, Jenkins M L, Hattar K, Edmondson P D and Roberts S G 2015 *Acta Mater.* **92** 163–77
[79] Yi X, Jenkins M L, Kirk M A, Zhou Z and Roberts S G 2016 *Acta Mater.* **112** 105–20
[80] El-Atwani O, Esquivel E, Efe M, Aydogan E, Wang Y Q, Martinez E and Maloy S A 2018 *Acta Mater.* **149** 206–19
[81] Yao Z, Jenkins M L, Hernández-Mayoral M and Kirk M A 2010 *Phil. Mag.* **90** 4623–34
[82] Arakawa K, Amino T and Mori H 2011 *Acta Mater.* **59** 141–5
[83] Arakawa K, Ono K, Isshiki M, Mimura K, Uchikoshi M and Mori H 2007 *Science* **318** 956–9
[84] Derlet P, Gilbert M and Dudarev S 2011 *Phys. Rev.* B **84** 134109
[85] Swinburne T D, Ma P-W and Dudarev S L 2017 *New J. Phys.* **19** 073024
[86] Marian J and Bulatov V V 2011 *J. Nucl. Mater.* **415** 84–95
[87] Terrier P, Athènes M, Jourdan T, Adjanor G and Stoltz G 2017 *J. Comput. Phys.* **350** 280–95
[88] Mason D R, Sand A E, Yi X and Dudarev S L 2018 *Acta Mater.* **144** 905–17
[89] Kirchheim R 2004 *Solid State Phys.* **59** 203–91
[90] Was G S *et al* 2017 *Nucl. Instrum. Methods Phys. Res.* B **412** 58–65
[91] Castin N, Dubinko A, Bonny G, Bakaev A, Likonen J, De Backer A, Sand A E, Heinola K and Terentyev D 2019 *J. Nucl. Mater.* **527** 151808
[92] Bakaev A, Zinovev A, Terentyev D, Bonny G, Yin C, Castin N, Mastrikov Y A and Zhurkin E E 2019 *J. Appl. Phys.* **126** 075110
[93] Gilbert M R, Dudarev S L, Derlet P M and Pettifor D G 2008 *J. Phys.: Condens. Matter.* **20** 345214
[94] Mason D R, Yi X, Sand A E and Dudarev S L 2018 *Europhys. Lett.* **122** 66001
[95] Bortz A B, Kalos M H and Lebowitz J L 1975 *J. Comput. Phys.* **17** 10–8
[96] Puchala B, Falk M L and Garikipati K 2010 *J. Chem. Phys.* **132** 134104
[97] Béland L, Brommer P, El-Mellouhi F, Joly J F and Mousseau N 2011 *Phys. Rev.* E **84** 046704
[98] Dederichs P H and Schroeder K 1978 *Phys. Rev.* B **17** 2524–36
[99] Hudson T S, Dudarev S L, Caturla M-J and Sutton A P 2005 *Phil. Mag.* **85** 661–75